J. Fluid Mech. (2009), *vol.* 621, *pp.* 155–182.
doi:10.1017/S0022112008004783 Printed in the United Kingdom

Boundary integral method for the evolution of slender viscous fibres containing holes in the cross-section

SRINATH S. CHAKRAVARTHY
AND WILSON K. S. CHIU†
Department of Mechanical Engineering, University of Connecticut, Storrs, CT 06269, USA

(Received 23 April 2007 and in revised form 16 October 2008)

We consider the evolution of slender viscous fibres with cross-section containing holes with application to fabrication of microstructured optical fibres. The fibre evolution is driven by either prescribing velocity or a force at the ends of the fibre, and the free surfaces evolve under the influence of surface tension, internal pressurization, inertia and gravity. We use the fact that ratio of the typical fibre radius to the typical fibre length is small to perform an asymptotic analysis of the full three-dimensional Navier–Stokes equations similar to earlier work on non-axisymmetric (but simply connected) fibres. A numerical solution to the multiply connected steady-state drawing problem is formulated based on the solution the Sherman–Lauricella equation. The effects of different drawing and material parameters like surface tension, gravity, inertia and internal pressurization on the drawing are examined, and extension of the method to non-isothermal evolution is presented.

1. Introduction

In this study, we aim to develop a model to predict the shape evolution of thin viscous fibres that contain holes in cross-section as they are drawn from an intial shape. Our motivation is the development of a relatively new class of optical fibres, the microstructured optical fibre. The cross-section of the microstructured optical fibre typically contains arrays of air holes that run through the length of the fibre. Such fibres are known as holey fibres, microstructured optical fibres, photonic crystal fibres (PCF), etc. These fibres have some distinct advantages to regular optical fibres, such as endless single mode propagation, large mode areas ranging over three orders of magnitude, photonic bandgaps at optical wavelengths, nonlinear effects such as supercontinuum generation, etc. (Birks *et al.* 1995; Birks, Knight & Russell 1997; Russel 2003). In addition to optical applications, these fibres have other uses also, such as atom-guiding fibres and other atomic transport and deposition processes. The range of applications described render it important to have precise control over the structure and size of holes along the entire length of the fibre.

Typically, as with most optical fibres, these fibres are produced by heating and drawing a preform (typically centimetres in diameter) down to the required diameter (typically 125 μm) with typical hole sizes between 10 nm and 10 μm. The preforms for PCFs may be manufactured in several ways, and some of the more common

† Email address for correspondence: wchiu@engr.uconn.edu

approaches are stacking capillaries around a solid rod, directly drilling the holes in the preform, or using sol–gel methods to produce the desired structure directly in the preform. Irrespective of the method of manufacturing the preform, the geometry of the final fibre is influenced by parameters such as draw-furnace temperature, drawing speed, feed speed, etc. When small-diameter holes are required, the high temperatures or low speeds can cause some of these holes to collapse due to surface tension. One possible method to reduce or control the collapse is to pressurize the holes from inside. It has been found that the process is extremely sensitive to the degree of pressurization and that some of the holes may even explode during drawing (Bise *et al.* 2002). Also, it may be necessary to control the collapse to produce holes with a very-fine-tuned diameter, closely packed holes or holes with very small diameters. In addition, the location and size of holes also have an impact on the mechanical performance of the fibre. We are interested in the shape evolution of the holes during the drawing of microstructured optical fibres and also to determine the effect of the different drawing parameters on collapse/explosion of holes. The main purpose of this study is to develop a numerical method capable of simulating the drawing process for a large variety of geometries and also to develop a phenomenological understanding of the mechanisms controlling fibre fabrication, thereby reducing the effort and cost in the most expensive part of fibre fabrication – preform preparation.

The drawing of conventional (solid) optical fibre has been studied extensively (Matovich & Pearson 1969; Shah & Pearson 1972; Paek & Bunk 1978; Schultz & Davis 1982; Choudhury & Jaluria 1998; Yin & Jaluria 2000; Cheng & Jaluria 2002). The flow in this process is typically axisymmetric and steady. Thus the axisymmetric Navier–Stokes equations and free-boundary conditions were taken as a starting point in the analysis. Considerable mathematical simplication can be made to the axisymmetric problem by utilizing the slenderness in the geometry, which is characterized by ϵ, defined by the inverse ratio of a typical cross-sectional dimension to the length. When ϵ is small ($O(10^{-3})$ for a typical optical fibre draw down process), expansion of the governing equations in terms of powers of ϵ leads to a greatly simplified model (see Matovich & Pearson 1969; Schultz & Davis 1982). Dewynne, Ockendon & Wilmott (1992) and Dewynne, Ockendon & Wilmott (1994) derived the equations governing the evolution of slender viscous fibres with non-axisymmetric solid cross-sections using systematic asymptotic methods. These studies were limited to cases where the cross-section evolves in a self-similar manner while undergoing translation, rotation and affine scaling in size, thus limiting the analysis to cases when the capillary number is large. More recently, Cummings & Howell (1999) have extended these models to predict the evolution of non-axisymmetric solid fibres for small capillary numbers. They have used a similar asymptotic approach to derive the governing equations, boundary conditions and kinematic conditions and have partially decoupled the axial deformation (stretching) from the in-plane deformations (sintering). They have then used a complex variable approach coupled with conformal mapping to arrive at a set of explicit solutions for a wide variety of geometries.

However, there are not many studies concerning the drawing of fibres with cross-section containing holes. The drawing of thin-walled capillaries was modelled by a few researchers Yarin, Gospodinov & Roussinov 1994; Gospodinov & Yarin 1997; Sarboh, Milinkovic & Debeljkovic 1998. Recently, Fitt *et al.* (2001, 2002) developed an axisymmetric model to investigate the drawing of glass capillaries, laying a foundation to analysing simple microstructured fibre drawing. They used an *asymptotic analysis* (with a leading-order analysis similar to that of Dewynne *et al.*) to arrive at a closed-form expression to determine neck-down shape and velocity profiles as a

function of the different parameters. Fitt *et al.* (2001, 2002) validated their model with experiments, and the results indicate that the predictions from the model were remarkably accurate. In Fitt's model, glass was modelled as a Newtonian fluid, and the ratio of viscosity to surface tension was adjusted to fit the theoretical results to the experimental data. The assumption of axisymmetry in the model has precluded the consideration of multiple-holed structures. More recently, Xue *et al.* (2005*a*, *b*, 2006) have used the finite-element method to analyse drawing of microstructured optical fibres. In a series of papers, they have analysed transient drawing, steady state drawing and the effect of material properties on the drawing of PCFs.

In this study, we consider a multiple-holed structure, non-dimensionalize the Navier–Stokes equations and arrive at a leading-order set of equations. In § 2, we extend the approach of Cummings & Howell (1999) to include multiply connected geometries. We also show that the evolution of the shape of the cross-section decouples into a plane Stokes flow problem with surface tension/pressure-driven boundaries coupled with a kinematic condition that governs the out-of-plane evolution. It should be pointed out that the shape of the cross-section is not known in advance and we have to solve the free-boundary problem to determine its evolution. This study will focus on geometries that are symmetric such that the centre of mass of each cross-section is fixed and does not move when the cross-section evolves and that no intial translation and twist have been applied to the fibre. We then use the complex variable approach to derive an integral equation that is used to solve the Stokes flow problem in the plane in § 3. The numerical scheme employed to determine the evolution of the cross-secion is discussed in § 4. In § 5, we show that for a trivial case of the drawing of an annular tube (capillary), the solution is essentially identical to that obtained by Fitt *et al.* (2002), and then present some sample numerical solutions to illustrate the effects of surface tension, inertia, gravity and to show that the model is capable of predicting hole collapse. In § 6, we present the technique to extend the numerical solution to non-isothermal drawing in which there is only an axial temperature distribution. Our conclusions and discussion of the implications of the numerical method to practical applications are given in § 7.

2. Mathematical Modelling

We consider the flow of a viscous jet or fibre, the geometry of which is schematically represented in figure 1. In modelling the problem, we employ a procedure similar to those of Dewynne *et al.* (1994) and Cummings & Howell (1999) to obtain the equations governing the evolution of the cross-section. We assume that the fibre is an incompressible Newtonian viscous fluid that is isothermal during the draw down process. The fluid flow is thus governed by the three-dimensional incompressible Navier–Stokes equations,

$$\nabla \cdot \boldsymbol{u} = 0, \tag{2.1a}$$

$$\rho[\boldsymbol{u}_t + \boldsymbol{u} \cdot \nabla \boldsymbol{u}] = -\nabla p + \mu \nabla^2 \boldsymbol{u} + \boldsymbol{F}, \tag{2.1b}$$

where, $\boldsymbol{u} = \{u, v, w\}$ is the velocity vector, $\boldsymbol{F}$ is the body force vector, μ is the constant dynamic viscosity, ρ is the constant density, p is the pressure, and the subscript t indicates differentiation with respect to time. We assume that there are $M + 1$ free surfaces in the fibre, each of which can be given by $G^{\alpha}(x, y, z) = 0$, $\alpha = 0 \ldots M$, where $\alpha = 0$ denotes the outer bounding surface. We denote all the in-plane contours of the surfaces $G^{\alpha} = 0$ by ∂G^{α}, the in-plane domain by D and the sum of the *in* plane contours by ∂G. Since each free surface is a streamline, the free-surface conditions

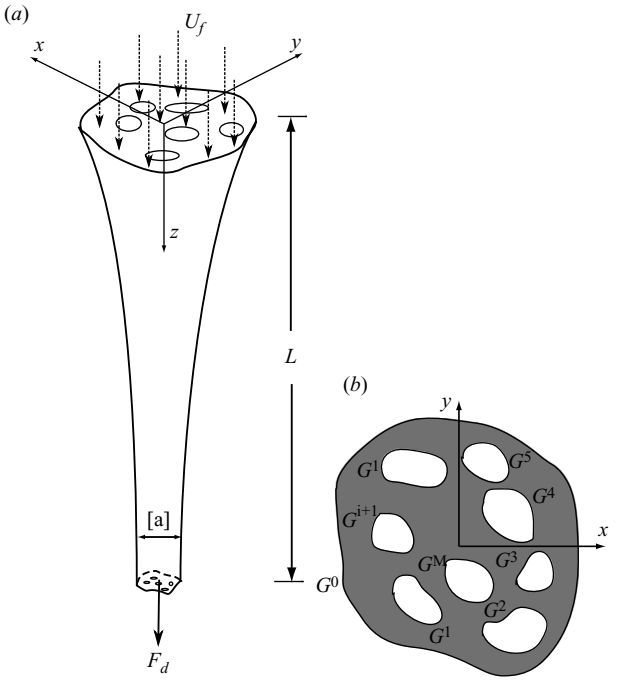

FIGURE 1. Schematisc of fibre drawing and the cross-sections: (*a*) schematic showing geometry and coordinate system for fibre drawing; and (*b*) schematic representation of geomatery showing the numbering of the different holes.

can be described by $M + 1$ kinematic conditions,

$$G_t^\alpha + \boldsymbol{u} \cdot \nabla G^\alpha = 0 \text{ on } G^\alpha(x, y, z) = 0. \tag{2.2}$$

It is assumed that these are surface tension and/or pressure-driven boundary problems. The free surface stress boundary conditions can be given by

$$\sigma \cdot \nabla G^\alpha = -\gamma \kappa^\alpha \nabla G^\alpha + P^\alpha \nabla G^\alpha \text{ on } G^\alpha(x, y, z) = 0, \tag{2.3}$$

where γ is the coefficient of surface tension, κ^α is the mean curvature of the interface, P^α is the magnitude of the internal pressurization on each surface, and σ is the stress tensor, the components of which are given by

$$\sigma_{ij} = -p\delta_{ij} + \mu \left(\frac{\partial u_i}{\partial x_j} + \frac{\partial u_j}{\partial x_i} \right),$$

where δ_{ij} is the Kronecker delta, and $i, j = 1 \ldots 3$. For steady-state drawing, the problem is closed by specifying the initial shape and the velocities at the ends of the fibre,

$$w = U_f \text{ at } z = 0, u = U_d \text{ at } z = L.$$

The problem can also be closed by prescribing a force at one end of the fibre and the shape and velocity at the other end. Let the largest typical dimension in the plane be $[a]$, for example the radius of the outer surface of the fibre. Now, we can define a parameter $\epsilon = [a]/L$, where L is a typical draw length. For typical optical fibre drawing conditions, $[a] \ll L$, such that $\epsilon \ll 1$. We will assume, henceforth, that ϵ is the small parameter in the problem. We non-dimensionalize and scale the problem

with

$$\boldsymbol{q} = U(\epsilon\bar{u}, \epsilon\bar{v}, \bar{w}), \quad \boldsymbol{x} = L(\epsilon\bar{x}, \epsilon\bar{y}, \bar{z}),$$
$$p = \frac{\mu U}{L}\bar{p}, \quad t = \frac{L}{U}\bar{t}, \quad G(x, y, z, t) = \bar{G}(\bar{x}, \bar{y}, \bar{z}),$$
$$\kappa = \frac{1}{\epsilon L}\bar{\kappa},$$

where U is a typical speed at which the fibre is drawn. In applying the following scaling, it is implicitly assumed that the fibre is nearly straight, the curvature of the centreline is small, and gravity is acting vertically along the axis. Non-dimensionalizing (2.1), we get

$$\bar{u}_{\bar{x}} + \bar{v}_{\bar{y}} + \bar{w}_{\bar{z}} = 0, \tag{2.4a}$$
$$\epsilon^2 Re(\bar{u}_{\bar{t}} + \bar{u}\bar{u}_{\bar{x}} + \bar{v}\bar{u}_{\bar{y}} + \bar{w}\bar{u}_{\bar{z}}) = -\bar{p}_{\bar{x}} + \bar{u}_{\bar{x}\bar{x}} + \bar{u}_{\bar{y}\bar{y}} + \epsilon^2\bar{u}_{\bar{z}\bar{z}}, \tag{2.4b}$$
$$\epsilon^2 Re(\bar{v}_{\bar{t}} + \bar{u}\bar{v}_{\bar{x}} + \bar{v}\bar{v}_{\bar{y}} + \bar{w}\bar{v}_{\bar{z}}) = -\bar{p}_{\bar{y}} + \bar{v}_{\bar{x}\bar{x}} + \bar{v}_{\bar{y}\bar{y}} + \epsilon^2\bar{v}_{\bar{z}\bar{z}}, \tag{2.4c}$$
$$\epsilon^2 Re(\bar{w}_{\bar{t}} + \bar{u}\bar{w}_{\bar{x}} + \bar{v}\bar{w}_{\bar{y}} + \bar{w}\bar{w}_{\bar{z}}) = -\epsilon^2\bar{p}_{\bar{z}} + \bar{w}_{\bar{x}\bar{x}} + \bar{w}_{\bar{y}\bar{y}} + \epsilon^2\bar{w}_{\bar{z}\bar{z}} + \epsilon^2 St. \tag{2.4d}$$

The non-dimensional boundary conditions are

$$(-\bar{p} + 2\bar{u}_{\bar{x}})\bar{G}^{\alpha}_{\bar{x}} + (\bar{u}_{\bar{y}} + \bar{v}_{\bar{x}})\bar{G}^{\alpha}_{\bar{y}} + (\epsilon^2\bar{u}_{\bar{z}} + \bar{w}_{\bar{x}})\bar{G}^{\alpha}_{\bar{z}} = (-\bar{\gamma}\bar{\kappa}^{\alpha} + \bar{P}^{\alpha})\bar{G}^{\alpha}_{\bar{x}}, \tag{2.5a}$$
$$(\bar{v}_{\bar{x}} + \bar{u}_{\bar{y}})\bar{G}^{\alpha}_{\bar{x}} + (-\bar{p} + 2\bar{v}_{\bar{y}})\bar{G}^{\alpha}_{\bar{y}} + (\epsilon^2\bar{v}_{\bar{z}} + \bar{w}_{\bar{y}})\bar{G}^{\alpha}_{\bar{z}} = (-\bar{\gamma}\bar{\kappa}^{\alpha} + \bar{P}^{\alpha})\bar{G}^{\alpha}_{\bar{y}}, \tag{2.5b}$$
$$(\bar{w}_{\bar{x}} + \epsilon^2\bar{u}_{\bar{z}})\bar{G}^{\alpha}_{\bar{x}} + (\bar{w}_{\bar{y}} + \epsilon^2\bar{v}_{\bar{z}})\bar{G}^{\alpha}_{\bar{y}} + \epsilon^2(-\bar{p} + 2\bar{w}_{\bar{z}})\bar{G}^{\alpha}_{\bar{z}} = \epsilon^2(-\bar{\gamma}\bar{\kappa}^{\alpha} + \bar{P}^{\alpha})\bar{G}^{\alpha}_{\bar{z}}. \tag{2.5c}$$

The non-dimensional kinematic conditions are

$$\bar{G}^{\alpha}_{\bar{t}} + \bar{u}\bar{G}^{\alpha}_{\bar{x}} + \bar{v}\bar{G}^{\alpha}_{\bar{y}} + \bar{w}\bar{G}^{\alpha}_{\bar{z}} = 0 \ \bar{G}^{\alpha} = 0 \tag{2.6}$$

where

$$Re = \frac{\rho U L}{\mu}, \ St = \frac{\rho g L^2}{\mu U}, \ \bar{\gamma} = \frac{1}{\epsilon Ca}, \ Ca = \frac{\mu U}{\gamma},$$

are the Reynolds number, Froude number and the capillary number, respectively.

2.1. *Orders of magnitude of terms in the equations*

We assume that Re and St are $O(1)$ in all the following derivations, and we further assume that the capillary number $Ca = O(\epsilon^{-1})$, such that the non-dimensional surfae tension coefficient $\bar{\gamma} = 1/\epsilon Ca = O(1)$. Finally, we assume that the non-dimensional internal pressure is $O(\epsilon^{-2})$. Without loss of generality, it can be assumed that the pressure on the outer bounding surface is 0 and the pressure on the holes is equal to the difference between the pressure on the holes and the outer surface (hole overpressure). This scaling suggests that unless the hole overpressure is within $O(\epsilon^2)$ of the ambient pressure, the holes would explode. These dimensionless numbers are chosen such that in the leading-order model, there is a balance between all the desired effects of viscosity inertia, gravity, surface tension and internal pressurizaiton. Thus the leading-order model obtained is the most general and applicable to a wide variety of flows where the geometry is slender. Thus, in summary, the entire problem is characterized by the following scaling of the dimensionless parameters:

$$Re = O(1), \ St = O(1), \ Ca = O(\epsilon^{-1}), \ \bar{P}^{\alpha} = O(\epsilon^{-2}). \tag{2.7}$$

The nature of the different physical effects can be now determined, and the correct leading-order equations can be easily determined by letting the appropriate dimensionless quantity tend to 0.

2.2. *Asymptotic analysis*

Our analysis is based on expansions of each of the scaled dependent variables $\bar{u}$, $\bar{v}$, $\bar{w}$, $\bar{p}$, $\bar{G}^{\alpha}$, $\bar{\kappa}^{\alpha}$, $\bar{P}^{\alpha}$ as the regular asymptotic series in even powers of ϵ, for example, $\bar{u} = \bar{u}_0 + \epsilon^2 \bar{u}_1 + O(\epsilon^4) \ldots$. Substituting the expansions in (2.4) and dropping the overbars, we obtain the leading-order non-dimensional governing equations to be

$$u_{0x} + v_{0y} + w_{0z} = 0, \tag{2.8a}$$

$$u_{0xx} + u_{0yy} = -p_{0x}, \tag{2.8b}$$

$$v_{0xx} + v_{0yy} = -p_{0y}, \tag{2.8c}$$

$$w_{0xx} + w_{0yy} = 0. \tag{2.8d}$$

The leading-order boundary conditions become

$$(-p_{0x} + 2u_{0x})G^{\alpha}_{0x} + (u_{0y} + v_{0x})G^{\alpha}_{0y} + w_{0x}G^{\alpha}_{0z} = \left(-\gamma\kappa^{\alpha}_0 + P^{\alpha}_0\right)G^{\alpha}_{0x}, \tag{2.9a}$$

$$(v_{0x} + u_{0y})G^{\alpha}_{0x} + (-p_{0y} + 2v_{0x})G^{\alpha}_{0y} + w_{0y}G^{\alpha}_{0z} = \left(-\gamma\kappa^{\alpha}_0 + P^{\alpha}_0\right)G^{\alpha}_{0y}, \tag{2.9b}$$

$$w_{0x}G^{\alpha}_{0x} + w_{0y}G^{\alpha}_{0y} = 0. \tag{2.9c}$$

The leading-order kinematic condition at each surface i is

$$G^{\alpha}_{0t} + u_0 G^{\alpha}_{0x} + v_0 G^{\alpha}_{0y} + w_0 G^{\alpha}_{0z} = 0 \text{ on } G^{\alpha}_0 = 0. \tag{2.10}$$

The leading-order axial velocity w_0 now satisfies (2.8d) along with the boundary conditions (2.9c). This represents a homogeneous Neumann problem which implies that w_0 is independent of x and y. This can be restated as

$$w_0 = w_0(z, t). \tag{2.11}$$

Equations (2.9) and (2.10) are exactly the same as in Dewynne *et al.* (1992) and Cummings & Howell (1999), except that we have conditions for each bounding surface. We can integrate the leading-order kinematic conditons (2.10) around the contour to get

$$\oint_{\partial G} \left(G^{\alpha}_{0t} + u_0 G^{\alpha}_{0x} + v_0 G^{\alpha}_{0y} + w_0 G^{\alpha}_{0z}\right) \frac{\mathrm{d}s}{|\nabla_s G^i_0|} = 0. \tag{2.12}$$

Applying the divergence theorem to (2.12) and (2.9c) and a form of Reynolds transport theorem introduced by Dewynne *et al.* (1994), we obtain

$$A_t + (w_0 A)_z = 0, \tag{2.13}$$

which represents the global conservation of mass, where A is the total cross-sectional area.

2.3. *Equations for the case with no surface tension*

We start the simplification process by considering the case when the surface tension is 0. The leading-order boundary conditions (2.9) reduce to

$$(-p_{0x} + 2u_{0x})G^{\alpha}_{0x} + (u_{0y} + v_{0x})G^{\alpha}_{0y} + w_{0x}G^{\alpha}_{0z} = 0 \text{ on } G^{\alpha}_0 = 0, \tag{2.14a}$$

$$(v_{0x} + u_{0y})G^{\alpha}_{0x}(-p_{0y} + 2v_{0x})G^{\alpha}_{0y} + w_{0y}G^{\alpha}_{0z} = 0 \text{ on } G^{\alpha}_0 = 0, \tag{2.14b}$$

$$w_{0x}G^{\alpha}_{0x} + w_{0y}G^{\alpha}_{0y} = 0 \text{ on } G^{\alpha}_0 = 0. \tag{2.14c}$$

The general solution to the leading-order cross-flow problem was found by Dewynne *et al.* (1994). We adopt the ZST notation to denote the solution for the leading-order

zero-surface-tension problem (see Cummings & Howell 1999):

$$u_{ZST} = x_t^* + w_0 x_z^* - \frac{(x - x^*)}{2} w_{0z} + c(z,t)(y - y^*), \tag{2.15a}$$

$$v_{ZST} = y_t^* + w_0 y_z^* - \frac{(y - y^*)}{2} w_{0z} + c(z,t)(x - x^*), \tag{2.15b}$$

$$p_{ZST} = -w_{0z}, \tag{2.15c}$$

where x^*, y^* represent the centre line of the fibre (line joining the centroid of each cross-section), and $c(z,t)$ represents the rotation in the (x,y) plane. The velocities are not unique because, the solution to the stress boundary value problem can be determined only up to an arbitrary rotation ($a(z,t)$) and rigid body translation ($b(z,t)$ and $c(z,t)$). From the form of (2.13) and (2.15) and with the argument from Dewynne *et al.* (1994), we can deduce that the cross-section of the fibre maintains its shape as it evolves. In general, the cross-section can translate, rotate and undergo affine size scaling as it evolves. For the problem of steady-state drawing of microstructured fibres, we limit our attention to cases when the inital velocity has only an axial component. For non-zero surface tension, (2.15) is no longer a solution because the lateral force imparted by the presence of surface-tension does not permit self-similar evolution.

2.4. *Case with surface tension*

When the surface tension is non-zero, we begin by rewriting (2.8*b*) and (2.8*c*) in terms of a stress function $\mathscr{U}$ such that $\mathscr{U}$ satisfies the biharmonic equation for the leading-order cross-flow problem. The problem can now be written in terms of $\mathscr{U}$ as

$$\nabla_s^4 \mathscr{U} = 0, \text{ in } S, \tag{2.16a}$$

$$\mathscr{U} = 0, \quad \frac{\partial \mathscr{U}}{\partial \boldsymbol{n_s}^\alpha} + \bar{\gamma} = \mathscr{C}^\alpha \cdot \boldsymbol{n_s}^\alpha \text{ on } \partial G^\alpha = 0, \tag{2.16b}$$

where $\boldsymbol{n_s}^\alpha$ is the normal vector $\mathscr{C}^\alpha$ is a constant vector. The calculation of $\mathscr{C}^\alpha$ will be discussed in § 3.1. The boundary value problem has to be solved for $\mathscr{U}$ at each time step as the cross-section evolves according to the kinematic conditions (2.10). If G^α are given, then $\mathscr{U}$ can be obtained uniquely. However, it is well known that for a stress booundary value problem, the cross-flow velocity gradients and pressure given by

$$p_0 = -\frac{1}{2}(\mathscr{U}_{xx} + \mathscr{U}_{yy}), \tag{2.17a}$$

$$u_{0x} = \frac{1}{4}(\mathscr{U}_{yy} - \mathscr{U}_{xx}) - \frac{1}{2} w_{0z}, \tag{2.17b}$$

$$v_{0y} = \frac{1}{4}(\mathscr{U}_{xx} - \mathscr{U}_{yy}) - \frac{1}{2} w_{0z}, \tag{2.17c}$$

do not determine the velocity components uniquely. An arbitrary rigid body motion can be added to the flow without changing the stress state. To determine the velocities uniquely and predict the evolution of the cross-section, we proceed to higher-order equations and find an equation for the axial stress balance of the fibre. In general, $\mathscr{U}$ has to be solved at every time step as the cross-section evolves to determine the evolution of the cross-section.

The first-order axial problem can be obtained from $O(\epsilon^2)$ terms in (2.4) and (2.5). They are

$$w_{1xx} + w_{1yy} = \nabla_s^2 w_1 = Re(w_{0t} - w_o w_{oz}) + p_{0z} - w_{0zz} - St \text{ in } A, \tag{2.18a}$$

$$w_{1x} G_{0x}^{\alpha} + w_{1y} G_{0y}^{\alpha} = \frac{\partial w_1}{\partial \boldsymbol{n_s}^{\alpha}} = G_{0z}^{\alpha}\left(p_0 - 2w_{0z} - \bar{\gamma}\kappa_0^{\alpha}\right) - G_{0x}^{\alpha} u_{0z} - G_{0y}^{\alpha} v_{0z} \text{ on } G_0^{\alpha} = 0. \tag{2.18b}$$

Integrating (2.18a) and applying the divergence theorem, we get

$$\int\int_D \nabla^2 w_1 \mathrm{d}A = \oint_{\partial G} \frac{\partial w_1}{\partial \boldsymbol{n_s}} \mathrm{d}s = \sum_{\alpha=0}^{M} \oint_{\partial G^{\alpha}} w_1 \cdot \boldsymbol{n_s}^{\alpha} \mathrm{d}s. \tag{2.19}$$

After some involved manipulations to evaluate the integrals in (2.19), we can arrive at the axial stress balance equation (similar to 3.11 in Cummings & Howell 1999)

$$(3Aw_{0z})_z = ReA(w_{0t} + w_o w_{oz}) - St - \frac{1}{2}\bar{\gamma}\Gamma_z - \sum_{\alpha=1}^{M} \frac{1}{2} \oint_{\partial G^{\alpha}} \mathscr{C}^{\alpha} \cdot \boldsymbol{n_s}^{\alpha} d\mathrm{s}, \tag{2.20}$$

where $A = \int\int_D \mathrm{d}x\mathrm{d}y = \int\int_{A^0} \mathrm{d}x\mathrm{d}y - \sum_{A^{\alpha}} \int\int_{A^{\alpha}} \mathrm{d}x\mathrm{d}y$ and $\Gamma = \sum_{\alpha=0}^{M} \oint_{\partial G^{\alpha}} \mathrm{d}s$. Equation (2.20) may be integrated to give

$$3Aw_{0z} = \overline{F_d} + \int ReA(w_{0t} + w_o w_{oz}) - StA - \frac{1}{2}\bar{\gamma}\Gamma - \int \sum_{\alpha=1}^{M} \frac{1}{2} \oint_{\partial G^{\alpha}} \mathscr{C}^{\alpha} \cdot \boldsymbol{n_s}^{\alpha} d\mathrm{s}. \tag{2.21}$$

In 2.21, $\overline{F_d}$ is the non-dimensional draw tension and is defined as

$$\overline{F_d} = \frac{F_d}{\mu U L \epsilon^2}, \tag{2.22}$$

where F_d is the applied draw tension. In summary, using the results in the literature, we have arrived at a system of equations, (2.13) and (2.20) for w_0, A and Γ of the microstructured fibre. When using these equations for a solid fibre, we can recover the closed system of equations of Cummings & Howell (1999). Also, in the limit when the surface tension goes to 0, the fibre maintains its shape as it evolves. However, for complicated geometries, the relationship between the areas and the circumference is not known. For cross-sections containing holes (multiply connected), these equations have no information about the evolution of each of the different surfaces ($G^{\alpha} = 0$). Also, in general, if the cross-section has no symmetry, the centre of mass of each cross-section will not be fixed as the fibre evolves. Thus, to make further progress, we need to determine the lateral translation and twist of the fibre from the first-order cross-flow equations and boundary conditions. Integration of the first-order cross-flow equations gives the lateral-force balance, and elimination of the velocities and the pressures gives us equations relating the first-order perturbation to the mean curvature of the free surface (κ_1), the shape of the cross-section, the surface tension and the leading-order axial velocity. These equations are not derived here, but the derivation is almost identical to that of Cummings & Howell (1999 p. 369, 3.13–3.15). It is worth pointing out that since these integrals involve the first-order curvature, the general solution to the problem is complicated and we do not attempt to solve for the lateral translation and twist. In this study, we will limit our attention to geometries that are symmetric, such that the centre of mass of each cross-section is fixed and does not move when the cross-section evolves and that no initial translation and twist

have been applied on the fibre. Before we proceed, it is worth noting that the form of (2.21) is not changed by the inclusion of internal pressurization in our equations.

3. Complex variable approach

We can transform the problem into a modified version of the purely two-dimensional (problem studied by Tanveer & Vasconcelos (1994, 1995). A very similar methodology was used by Cummings & Howell (1999) and Howell & Siegel (2004). We will first solve the leading-order cross-flow problem (2.17) and use the solution to derive equations for the evolution of the cross-section. Throughout this section, we drop the suffices on the the leading-order variables. We first subtract the zero-surface-tension homogeneous solution by setting

$$p = p_{ZST} + \tilde{p}, \quad u = u_{ZST} + \tilde{u}, \quad v = v_{ZST} + \tilde{v}.$$

Due to the definitions above, the cross-section has no net linear or angular momentum with respect to $\tilde{u}$ and $\tilde{v}$, and they satisfy

$$\int\int_A \begin{pmatrix} \tilde{u} \\ \tilde{v} \end{pmatrix} \mathrm{d}x\,\mathrm{d}y = 0, \tag{3.1a}$$

$$\int\int_A ((x - x^*)\tilde{v} - (y - y^*)\tilde{u})\,\mathrm{d}x\,\mathrm{d}y = 0. \tag{3.1b}$$

In terms of the new variables, the leading-order cross-flow problem becomes

$$\tilde{u}_x + \tilde{v}_y = 0, \tag{3.2a}$$

$$\tilde{u}_{xx} + \tilde{u}_{yy} = \tilde{p}_x, \tag{3.2b}$$

$$\tilde{v}_{xx} + \tilde{v}_{yy} = \tilde{p}_y, \tag{3.2c}$$

$$(-\tilde{p}_x + 2\tilde{u}_x)_x + (\tilde{u}_y + \tilde{v}_x)_y = (-\gamma\kappa^\alpha + P^\alpha)_x \text{ on } G^\alpha = 0, \tag{3.2d}$$

$$(\tilde{v}_x + \tilde{u}_y)_x + (-\tilde{p}_y + 2\tilde{v}_x)_y = (-\gamma\kappa^\alpha + P^\alpha)_x \text{ on } G^\alpha = 0. \tag{3.2e}$$

Equation (3.2) is the same as the problem of two-dimensional Stokes flow with a surface tension-driven boundary. The evolution of the cross-section is determined by the kinematic condition:

$$\begin{aligned} G^\alpha_t + \tilde{u}G^\alpha_x + \tilde{v}G^\alpha_y = -wG^\alpha_z + \frac{1}{2}w_z((x - x^*)G^\alpha_x + (y - y^*)G^\alpha_y) \\ + (x^*_t + wx^*_z)G^\alpha_x - (y^*_t + wy^*_z)G^\alpha_y \quad \text{on } G^\alpha = 0. \end{aligned} \tag{3.3}$$

Equation (3.3) is the same as (4.3), p. 371, of Cummings & Howell (1999), except for the superscripts accounting for each of the free surfaces. The right-hand side of (3.3) for a classical two-dimensional Stokes flow problem is 0. The extra terms account for flow from a cross-section upstream to a cross-section downstream as can be seen from the terms involving the axial velocity and for translation and rotation of the cross-section. As mentioned earlier, we will limit our attention to symmetric systems in which the centreline of the fibre remains fixed. We choose it such that the centreline lies on the z-axis so that

$$\begin{pmatrix} x^* \\ y^* \end{pmatrix} = \int\int_A \begin{pmatrix} x \\ y \end{pmatrix} \mathrm{d}x\,\mathrm{d}y = \begin{pmatrix} 0 \\ 0 \end{pmatrix}. \tag{3.4}$$

Using (3.4), the kinematic condition (3.3) can be modified to

$$G_t^\alpha + \tilde{u}G_x^\alpha + \tilde{v}G_y^\alpha = -wG_z^\alpha + \frac{1}{2}w_z\left(xG_x^\alpha + yG_y^\alpha\right) \text{ on } G^\alpha = 0. \tag{3.5}$$

Since we have reduced the problem to a Stokes flow problem with surface tension-driven boundaries coupled with a modified kinematic condition, methods applicable to multiply-connected stokes flow problems can be used to solve the leading-order cross-flow probem. Hopper (1990) and Richardson (1992) have shown that exact solutions to the plane Stokes flow problem for a simply connected region (right-hand side of (3.3) being indentically 0) may be found in terms of a time-dependent conformal map from a unit circular disc onto the cross-section. Cummings & Howell (1999) then extended these ideas to the problem of evolution of a non-axisymmetric slender jet. Tanveer & Crowdy (1998) and Richardson (2000) have independently found a class of exact conformal mapping solutions to the plane Stokes flow problem for the case of doubly connected fluid regions. For domains with higher connectivity, Vorst (1993) has obtained a numerical solution based on a boundary element method and has proposed a class of exact solutions for the plane Stokes flow problem. In this section, we adapt ideas from the literature and adapt them to provide a boundary integral-based numerical solution to our problem.

We start by defining a stream function ψ such that the velocity components can be written as

$$\tilde{u} = \psi_y, \tilde{v} = \psi_x.$$

From (3.2*a*), (3.2*b*) and (3.2*c*), ψ must satisfy the biharmonic equation and can, therefore, be expressed as

$$\psi = -\Im[\bar{\mathscr{Z}}\phi(\mathscr{Z}) + \chi(\mathscr{Z})], \tag{3.6}$$

where, the *Goursat functions* $\phi(\mathscr{Z})$ and $\chi(\mathscr{Z})$ are analytic everywhere in the fluid region $D(z, t)$; $\mathscr{Z} = x + \mathrm{i}y$ is the complex variable. All the physical quantities can be written in terms of these functions:

$$\tilde{u} + \mathrm{i}\tilde{v} = \phi(\mathscr{Z}) - \mathscr{Z}\overline{\phi'(\mathscr{Z})} - \overline{\chi'(\mathscr{Z})}, \tag{3.7a}$$

$$\tilde{\sigma_x} + \tilde{\sigma_y} = \tilde{p} = -4\mathrm{Re}[\phi'(\mathscr{Z})]. \tag{3.7b}$$

The stress boundary conditions of (3.2*d*) and (3.2*e*) can be combined to give

$$\phi(\mathscr{Z}) + \mathscr{Z}\overline{\phi'(\mathscr{Z})} + \overline{\chi'(\mathscr{Z})} = \mathrm{i}\frac{\bar{\gamma}}{2}\mathscr{Z}_s - P^\alpha\mathscr{Z} + \mathscr{C}^\alpha \text{ on } G^\alpha = 0, \tag{3.8}$$

where the primes indicate differentiation with respect to $\mathscr{Z}$, the subscript s stands for differentiation with respect to the arc length, and $\mathscr{C}^\alpha$ are constants of integration and the same as the constants defined in (2.16*b*). Thus, the problem is reduced to determining the analytic functions $\phi(\mathscr{Z})$ and $\chi'(\mathscr{Z})$. At each instance of time and axial location, the domain and the boundary conditions determine $\phi(\mathscr{Z})$, $\chi'(\mathscr{Z})$ and the constants $\mathscr{C}^\alpha$. In general, the constants $\mathscr{C}^\alpha$ are different, are not known *a priori* and must be determined as part of the solution process. However, without loss of generality, it can be assumed that $\mathscr{C}^0 = 0$. The calculation of $\mathscr{C}^\alpha$ will be discussed in § 3.1. The kinematic condition can also be converted to complex variable notation as:

$$\mathrm{Im}\left[\left(\tilde{u} + \mathrm{i}\tilde{v} - \mathscr{Z}_t + w\mathscr{Z}_z - \frac{1}{2}w_z\mathscr{Z}\right)\overline{\mathscr{Z}_s}\right] = 0 \text{ on } G^\alpha = 0 \tag{3.9}$$

Using (3.9) along with (3.7*a*) we obtain the kinematic condition in terms of the analytic function $\phi(\mathscr{Z})$ as :

$$\mathrm{Im}\left[\left(2\phi(\mathscr{Z}) - \mathscr{Z}_t - \mathrm{i}\frac{\bar{\gamma}}{2}\mathscr{Z}_s + P^\alpha \mathscr{Z} + w\mathscr{Z}_z - \frac{1}{2}w_z\mathscr{Z}\right)\overline{\mathscr{Z}_s}\right] = 0 \text{ on } G^\alpha = 0 \quad (3.10)$$

Equation (3.10) combined with combined with (2.13) and (2.20) determines the evolution of the cross-section, once $\phi(\mathscr{Z})$ is known. The general solution procedure is to determine $\phi(\mathscr{Z})$ for a given domain $D(z,t)$ and solve (3.10), (2.13) and (2.20) to obtain the cross-section at the next time step. We use the Sherman–Lauricella (S–L) integral equation to determine the analytic functions ϕ and χ' that govern the evolution of the cross-section.

3.1. *Sherman–Lauricella integral equation*

To find the analytic functions that satisfy the stress boundary value problem of (3.8), the S–L (see Muskhelishvili 1963*b*) equation is derived by letting $\phi(\mathscr{Z})$ and $\chi'(\mathscr{Z})$ take the form

$$\phi(\mathscr{Z}) = \frac{1}{2\pi\mathrm{i}}\oint_{\partial G}\frac{\omega(\eta)}{\eta - \mathscr{Z}}\mathrm{d}\eta + \sum_{\alpha=1}^{M}\frac{b_\alpha}{\mathscr{Z} - \mathscr{Z}_\alpha}, \quad (3.11a)$$

$$\chi'(\mathscr{Z}) = \frac{1}{2\pi\mathrm{i}}\oint_{\partial G}\frac{\overline{\omega(\eta)}\mathrm{d}t + \omega(\eta)\mathrm{d}\eta}{\eta - \mathscr{Z}} - \frac{1}{2\pi\mathrm{i}}\oint_{\partial G}\frac{\bar{\eta}\omega(\eta)}{(\eta - \mathscr{Z})^2}\mathrm{d}t + \sum_{\alpha=1}^{M}\frac{b_\alpha}{\mathscr{Z} - \mathscr{Z}_\alpha}. \quad (3.11b)$$

By letting $\mathscr{Z}$ tend to a point t_o on one of the contours, we can obtain the S–L integral equation:

$$\omega(t_o) + \frac{1}{2\pi\mathrm{i}}\oint_{\partial G}\omega(\eta)\mathrm{d}\,\log\left(\frac{\eta - t_o}{\bar{\eta} - \bar{t}_o}\right) - \frac{1}{2\pi\mathrm{i}}\oint_{\partial G}\overline{\omega(\eta)}\mathrm{d}\frac{\eta - t_o}{\bar{\eta} - \bar{t}_o}$$
$$+ \sum_{\alpha=0}^{M}\frac{b_\alpha}{t - \mathscr{Z}_\alpha} + \frac{b_\alpha}{\bar{t}_o - \overline{\mathscr{Z}_\alpha}}\left(1 - \frac{t_o}{\bar{t}_o - \overline{\mathscr{Z}_\alpha}}\right) - \mathscr{C}^\alpha = g(t_o). \quad (3.12)$$

where $\omega(\eta)$ is the density function, which is defined in (3.11), $b_\alpha = \mathrm{i}\int_{\partial G^\alpha}\omega(\eta)\mathrm{d}\bar{\eta} - \overline{\omega(\eta)}\mathrm{d}\eta, \alpha = 1\ldots M$ are real constants, $\mathscr{Z}_\alpha$ are arbitrary points inside each domain, and $\mathscr{Z}_0$ is chosen such that it lies in D, $\mathscr{C}^\alpha = \int_{L_\alpha}\omega(\eta)\mathrm{d}\eta$ are the arbitrary constants in (3.8) and $g(t_o)$ is equal to the right-hand side of (3.8) evaluated at a boundary point t_o. Although $\mathscr{C}^\alpha$ are not known *a priori*, they can be replaced by the integrals $\mathscr{C}^\alpha = \int_{\partial G^\alpha}\omega(\eta)\mathrm{d}\eta$ and determined during the solution of the S–L integral equation (Muskhelishvili 1963*b*; Lu 1995). The addition of imaginary constant $b_0 = \mathrm{i}\int_{\partial G}((\omega(\eta))/(\eta - \mathscr{Z}_0))\,\mathrm{d}\eta - (\overline{\omega(\eta)})/(\bar{\eta} - \bar{\mathscr{Z}}_0))\,\mathrm{d}\bar{\eta}$ serves to convert the S–L equation into a pair of Fredholm equations of the second kind for the real and imaginary parts of $\omega(\eta)$. It can be proved that $b_0 = 0$ is a necessary condition for the existence of a solution to the S–L equation. Readers are refered to Muskhelishvili (1963*b*,*a*) for further details. The S–L equation is particularly attractive for solution because the kernels are continuous along each component of the boundary, it is readily extensible to domains that are multiply-connected, and recent advancement into numerical methods has shown that the S–L equation can be solved in $O(N)$ (where N is the number of points used in discretizing the boundary) operations for large problems using the Fast Multipole Method (FMM). This renders the solution of this form particularly useful in solving moving boundary value problems. This approach has been used by Crowdy (2002) to solve for the viscous sintering in multiply connected domains. The equation listed above is the general form of the S–L equation. Although

the numerical solution to the problem can be obtained, the problem size and the complexity can be considerably reduced by the use of symmetry. As mentioned earlier, only problems with *cyclic symmetry* are studied here and the S–L equation is modified to reflect this symmetry.

3.2. *Cyclic symmetry*

For problems possessing *cyclic symmetry*, the domain and the boundary conditions are invariant when the domain is rotated by an angle $\theta = \frac{2\pi}{n}$ ($n \geqslant 2$ is an integer) about the origin. Such a domain is characterized by an outer bounding contour, possibly an inner bounding contour and possibly m holes (closed contours, $m < M$) in each basic region. The properties of the complex stress function and the modified version of the S–L equation are presented here. Consider the transformation $\mathscr{Z} \longmapsto \mathfrak{z}$ such that $\mathfrak{z} = \mathscr{Z}\mathrm{e}^{\mathrm{i}\theta}$ corresponding to a rotation of θ about the origin. Invariance of the stress and the velocity fields due to rotation of θ implies from (3.7) that

$$\phi(\mathfrak{z}) = \mathrm{e}^{\mathrm{i}\theta}\phi(\mathscr{Z}), \tag{3.13a}$$

$$\chi'(\mathfrak{z}) = \mathrm{e}^{-\mathrm{i}\theta}\chi'(\mathscr{Z}), \tag{3.13b}$$

$$\phi'(\mathfrak{z}) = \phi'(\mathscr{Z}). \tag{3.13c}$$

Following Mikhailov (1979), we shall ignore the second term of (3.12) so that the density function $\omega(t_o)$ possesses the same symmetry of $\phi(\mathscr{Z})$ and the subsequent derivation of the modified integral equation poses no difficulties. Thus, it is relatively simple to prove that the symmetry conditions of (3.13) will hold if

$$\omega(\eta\mathrm{e}^{\mathrm{i}\theta}) = \mathrm{e}^{\mathrm{i}\theta}\omega(\eta). \tag{3.14}$$

Let ∂G^{p0}, $p = 0 \ldots m$, represent the contours of G^{α}, $\alpha = 0 \ldots M$, lying within the angle $0 \leqslant \theta \leqslant 2\pi/n$, and let $\partial G^{00}$and ∂G^{m0} represent the outer and inner bounding contours, respectively. Let ∂G^{pk} represent the contour obtained by rotating ∂G^{p0} by an angle $\theta_k = 2\pi k/n$, $k = 0 \ldots n-1$. Using (3.13) and (3.14), we can rewrite the S–L equation in the form

$$\omega(t_o) + \frac{1}{2\pi\mathrm{i}}\sum_{k=0}^{n-1}\sum_{p=0}^{m}\left\{\int_{\partial G^{pk}}\omega(\eta)\,\mathrm{dlog}\left(\frac{\eta - t_o}{\bar{\eta} - \bar{t}_o}\right) - \int_{\partial G^{pk}}\overline{\omega(\eta)}\mathrm{d}\frac{\eta - t_o}{\bar{\eta} - \bar{t}_o}\right\}$$
$$+ \mathrm{i}\sum_{k=0}^{n-1}\sum_{p=0}^{m}\int_{\partial G^{pk}}\frac{\omega(\eta)\mathrm{d}\bar{\eta} - \overline{\omega(\eta)}\mathrm{d}\eta}{\bar{t}_o - \overline{\mathscr{Z}_{pk}}} - \mathscr{C}^{l0} = g(t_o),\ t_o \in \partial G^{l0}. \tag{3.15}$$

where $\mathscr{Z}_{pk}$ is the point $\mathscr{Z}_{\alpha}$ in (3.12), and by definition $\mathscr{Z}_{pk} = \mathrm{e}^{\mathrm{i}\theta_k}\mathscr{Z}_{p0}$. Introducing a change of variables $\tau = \eta\mathrm{e}^{-\mathrm{i}\theta_k}$, we have for $\eta \in \partial G^{pk}$, $\omega(\eta) = \omega(\tau)\mathrm{e}^{\mathrm{i}\theta_k}$, thereby transforming ∂G^{pk} into ∂G^{p0}. Denote ∂G as the sum of all contours ∂G^{p0} (3.15) can be written as

$$\omega(t_o) + \frac{1}{2\pi\mathrm{i}}\sum_{k=0}^{n-1}\left\{\int_{\partial G}\omega(\eta)\mathrm{e}^{\mathrm{i}\theta_k}\mathrm{dlog}\left(\frac{\eta\mathrm{e}^{\mathrm{i}\theta_k} - t_o}{\bar{\eta}\mathrm{e}^{-\mathrm{i}\theta_k} - \bar{t}_o}\right) - \int_{\partial G}\overline{\omega(\eta)}e^{\mathrm{i}\theta_k}\mathrm{d}\frac{\eta\mathrm{e}^{\mathrm{i}\theta_k} - t_o}{\bar{\eta}\mathrm{e}^{-\mathrm{i}\theta_k} - \bar{t}_o}\right\}$$
$$+ \mathrm{i}\sum_{k=0}^{n-1}\int_{\partial G}\frac{\omega(\eta)\mathrm{d}\bar{\eta} - \overline{\omega(\eta)}\mathrm{d}\eta}{\bar{t}_o - \overline{\mathscr{Z}_{p0}}\mathrm{e}^{-\mathrm{i}\theta_k}} - \mathscr{C}^{l0} = g(t_o),\ t_o \in \partial G^{l0}, \tag{3.16}$$

where $\mathscr{C}^{l0} = \int_{\partial G^{l0}} \omega(\eta) \mathrm{d}s$, $\mathscr{C}^0 = 0$ and $\mathscr{C}^m = 0$ from symmetry. Finally, using (3.13) in (3.8), we can obtain

$$\mathscr{C}^{lk} = \mathrm{e}^{\mathrm{i}\theta_k} \mathscr{C}^{l0}, \; k > 0. \tag{3.17}$$

Substituting (3.17) in (2.20), the last integral can now be written as

$$\sum_{p=0}^{m} \sum_{k=0}^{n-1} \int_{\partial G^{pk}} \mathrm{e}^{\mathrm{i}\theta_k} \mathscr{C}^{p0} \cdot \mathbf{n}_{\mathbf{s}} \, \mathrm{d}s.$$

However, $\sum_{k=0}^{n-1} \mathrm{e}^{\mathrm{i}\theta_k} = 0$; therefore, (2.20) for rotationally symmetric systems is

$$(3A w_{0z})_z = ReA(w_{0t} + w_o w_{oz}) - StA - \frac{1}{2}\bar{\gamma}\Gamma_z. \tag{3.18}$$

An additional term similar to b_0 in (3.12) has to be added to (3.16) in order to make it uniquely solvable. The kernels for the symmetric version of the S–L equation are also smooth and can be evluated using the same procedure.

4. Numerical procedure

The numerical procedure to solve for the evolution of microstructured fibre is as follows. For a given initial geometry, the analytic funciton $\phi(\mathscr{Z})$ is determined by solving the S–L equation (3.12). We follow the formulation of Greengard, Kropinski & Mayo (1996) to solve the S–L equation. The formulation uses a set of N_α points, equally spaced with respect to some parametrization arc length (s in the present context), on each contour of ∂D_α. The S–L equation is discretized using the Nystrom method based on the trapezoidal rule since it achieves superalgebraic convergence for smooth data. The result of the discretization is a system of $2N$ linear equations of the form

$$\mathbf{H}\boldsymbol{\omega} = \boldsymbol{g}. \tag{4.1}$$

where $\mathbf{H}$ is a $2N \times 2N$ full matrix, $\boldsymbol{\omega}$ is the vector of density functions at each of the discretization points, and $\boldsymbol{g}$ represents the discretized vector of the right-hand side of the S–L equation. Greengard *et al.* (1996) use the FMM combined with the Generalized Minimum Residual Method (GMRES)-iterative solver to solve the matrix equaitons in (4.1) to the find the unknown density function vector ω in $O(N)$ operations. In the current application, we use either direct inversion using Gaussian Elimination or the GMRES-iterative method without fast multipole acceleration to demonstrate the capability in modelling the complex three-dimensional evolution of the fibre. For problems involving a large number of holes, the FMM combined with the GMRES-iterative solver requiring $O(N)$ operations can be used to solve the matrix equations in 4.1 to find the unknown density function ω (Greengard *et al.* 1996). Once the density function $\omega(t)$ is determined, (3.11) is used to determine $\phi(\mathscr{Z}_k)$, $k = 1 \ldots N \times M$ at each of the boundary points.

Once the analytic function $\phi(\mathscr{Z}_k)$ is determined, (2.13), (2.20) and (3.10) now need to be solved to determine the evolution of the current cross-section. These equations now represent a set of $2N$ coupled ordinary differential equations (ODEs) governing the evolution of each of the N boundary points. In this paper, we are interested only in the steady-state evolution of the cross-section of the fibres, although the numerical method presented here can be easily adapted to study the unsteady (transient) evolution of the fibres. Provided the draw force (F_d) is given, or if we have good estimate of the axial velocity derivative ($w_z(z=0)$) at the start, an explicit method

can be used to determine the evolution of the fibre. In our formulation, we use a fourth-order explicit Runge–Kutta method with adaptive time stepping (where the time steps correspond to steps along the axial direction) to solve the set of ODEs.

After every iteration (time step), a piecewise cubic spline is fit through the newly obtained boundary points to determine the first derivative and the second derivative (curvature κ) of the boundary with respect to the arc lengh (s), since the solution of the S–L equation relies on the availability of these quantities. A general algorithm was developd to redistribute the boundary points along the boundary of each contour based on the equidistribution pricinple (see Thompson 1985), where any non-uniform point distribution can be considered to be a transformation, $x(\zeta)$, from a uniform grid in ζ-space. This process is accomplished using a weight function $\beta(\zeta)$ that satisfies

$$\frac{\partial x}{\partial \zeta}\beta(\zeta) = \text{constant}. \tag{4.2}$$

The equidistribution is accomplished by solving the Euler equation for the minimization of the integral

$$I = \int \beta(\zeta) x_\zeta^2 \, \mathrm{d}\zeta. \tag{4.3}$$

After every iteration, the boundary points are redistributed such that the arc length between successive boundary points is equal so that the trapezoidal rule or any higher-order Newton–Cotes type of formula for equally spaced points can be used to perform the integrations necessary when solving the S–L equation. If a change in connectivity caused by complete collapse of small holes occurs, as defined when the ratio of the current area of the hole to its original area is less than 10^{-8}, this can be handled by simply removing this boundary from the cross-section and solving (4.1) once again. Due to small numerical errors in the piecewise cubic spline fitting, we observe oscillations in the derivatives even if the points have deviated minimally from a smooth curve. Least-squares b-spline smoothing is performed after every five iterations to avoid such oscillations. The boundary points are then redistributed according to the curvature (closer in regions of high curvature) using a general adaptive remeshing algorithm. The redistribution, spline interpolation and computation of the first derivative and curvature can all be accomplished in $O(N)$ operations, thus not being a significant bottleneck to the computations.

5. Results and discussion

In this section, we show the numerical results for the steady state evolution of the microstructured fibres, using the integral equation formulation described in §4. We simulate a number of example geometries to show the applicability of the method to practical problems involving the manufacturing of optical fibres that contain holes in the cross-section. From the governing equations, it is obvious that the stretching and the sintering processes are weakly coupled at best and possibly completely uncoupled from each other. We then examine the effect of the different parameters such as feed speed, draw force, draw speed, surface tension coefficient and the viscosity (and as a consequence temperature) on the evolution of the microstructure as it evolves. We will show that in the small surface tension limit, the surface tension effects are limited to a particular length during the drawing, beyond which the microstructure will evolve in an almost self-similar manner. We will also demonstrate that our method is capable of capturing the collapse of small holes and to continue simulating the

drawing process beyond the collapse of some of these holes. Finally, we will examine the effects of internal pressurization to show that, in some cases, the holes can start expanding and cause explosion and destruction of the fibre geometry. All simulations were performed on a single Intel Itanium 2 GHz processor with 1 GB RAM. Since the total mass should always be conserved, the velocity multiplied by the area at each iteration should be a constant. The maximum error of this quantity was always less than 0.5 % for all iterations and simulations. The most involved simulation on four holes using the GMRES-iterative solver with 1000 boundary points (125 boundary points for each hole and 500 boundary points for the outer surface) requires 1 minute per time step for a total of 6000 steps. The number of operations for GMRES without fast multipole acceleration scales with $O(N^2)$, where N is the number of boundary points. If one is interested in simulating a large number of holes, GMRES with fast multipole acceleration (Greengard *et al.* 1996) is recommended since it scales as $O(N)$; direct inversion by Gaussian Elimination is not recommended since it scales with $O(N^3)$.

5.1. *Validation of numerical solution (drawing of a capillary)*

The first example under consideration is the evolution of an annular cylinder, the cross-section of which is a circular disk with a circular hole located at the centre of the disk (origin). We will first show that the current methodology yields the same governing equations obtained by Fitt *et al.* (2002). Secondly, we will compare the numerical solution to the analytical perturbation solution of Fitt *et al.* (2002) under the small surface tension limit. This example will serve to demonstrate the accuracy and the speed of the method. We denote $R_o(z)$ and $R_i(z)$ as the outer and inner radii of the cylinder during the drawing process, and p_i as the overpressure on the inner cylinder. The solution for a circular annulus subjected to internal and external pressures can be found from the plane theory of elasticity; an accessible proof of this result can be found in Muskhelishvili (1963*b*). For the problem under consideration (surface tension and internal pressurization), this result can be modified to

$$\phi(\mathscr{Z}) = \frac{-\gamma(R_o + R_i)}{2\left(R_o^2 - R_i^2\right)}\mathscr{Z} + \frac{p_i R_i^2}{2\left(R_o^2 - R_i^2\right)}\mathscr{Z}, \tag{5.1a}$$

$$\chi'(\mathscr{Z}) = \left\{ -\frac{\gamma(R_i + R_o)R_i R_o}{\left(R_o^2 - R_i^2\right)} + \frac{p_i R_o^2 R_i^2}{\left(R_o^2 - R_i^2\right)} \right\} \frac{1}{\mathscr{Z}}, \tag{5.1b}$$

Substituting for ϕ, χ' from (5.1), $A = \pi(R_o^2 - R_i^2)$ and $\Gamma = 2\pi(R_o + R_i)$ into (3.7*a*), (3.9) and (2.20), we obtain

$$\left(R_i^2 w_0\right)_z = \frac{p_i R_i^2 R_o^2 - \gamma R_i R_2 (R_i + R_o)}{\mu\left(R_o^2 - R_i^2\right)}, \tag{5.2a}$$

$$\left(R_o^2 w_0\right)_z = \frac{p_i R_i^2 R_o^2 - \gamma R_i R_2 (R_i + R_o)}{\mu\left(R_o^2 - R_i^2\right)}, \tag{5.2b}$$

$$\rho\left(R_o^2 - R_i^2\right)[w_0 w_{0z} - g] = \left[3\mu\left(R_o^2 - R_i^2\right)w_{0z} + \gamma(R_0 + R_i)\right]_z. \tag{5.2c}$$

Equation (5.2) are identical to the steady-state version of (19) – (21) of Fitt *et al.* (2002). Under the small surface tension limit with no inertial and gravitational effects, Fitt *et al.* (2002) used a perturbation solution to solve (5.2) and obtained for the

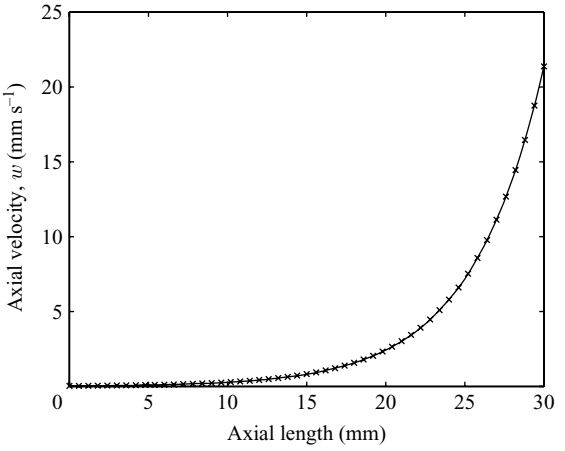

FIGURE 2. Comparison between the numerically obtained axial velocity profile (symbols) to the analytical solution (line).

boundary conditions $R_o(0) = R_{o0}$, $R_i(0) = R_{i0}$, $w_o(0) = U_f$(feed speed) and $w_0(L) = U_d$ (draw speed)

$$R_o = R_{o0}\, e^{\frac{\beta z}{-2L}} + \frac{\gamma L e^{-\frac{\beta z}{L}}}{3\mu\beta U_f (R_{o0} - R_{i0})} \left[(3R_{i0} - R_{o0})\left(1 - e^{-\frac{\beta z}{2L}}\right) + \left(\frac{R_{o0} z}{L}\right) e^{\frac{\beta z}{2L}} \left(e^{-\frac{\beta}{2}} - 1\right) \right], \quad (5.3a)$$

$$R_i = R_{i0} e^{-\frac{\beta z}{2L}} + \frac{\gamma L e^{-\frac{\beta z}{L}}}{3\mu\beta U_f (R_{o0} - R_{i0})} \left[(3R_{o0} - R_{i0})\left(1 - e^{-\frac{\beta z}{2L}}\right) + \left(\frac{R_{i0} z}{L}\right) e^{\frac{\beta z}{2L}} \left(e^{-\frac{\beta}{2}} - 1\right) \right], \quad (5.3b)$$

$$w_0 = U_f e^{\frac{\beta z}{L}} + \frac{2\gamma L e^{\frac{\beta z}{L}}}{3\mu\beta (R_{o0} - R_{i0})} \left[e^{-\frac{\beta z}{2L}} - 1 + \left(\frac{z}{L}\right)\left(1 - e^{-\frac{\beta}{2}}\right) \right] \quad (5.3c)$$

where $\beta = \ln(U_d / U_f)$.

A numerical solution was obtained with the initial and outer radii set to 12 and 14 mm, respectively. The feed speeds and the draw feeds were fixed at $U_f = 2\,\text{mm min}^{-1}$ and $U_d = 1300\,\text{mm min}^{-1}$ and the draw length was fixed to 30 mm. Figure 2 shows the comparison between the numerically obtained axial velocity and the velocoity from (5.3*c*). The maximum error between the numerically obtained axial velocity and the analytical solution was found to be less than 1 %. Figure 3 shows the comparison between the numerically obtained evolution of the inner and outer radii and the analytical solution. Once again the agreement between the analytical and the numerical solutions is very good, and the maximum error is less than 1 %. For this numerical solution, the outer and inner boundaries were each discretized using 150 points and the maximium axial space step was set to 0.06 mm. In figures 2 and 3, the symbols represent the numerical solution and the line represents the analytical solution. For ease of display, the numerical solution is shown in steps of 0.6 mm.

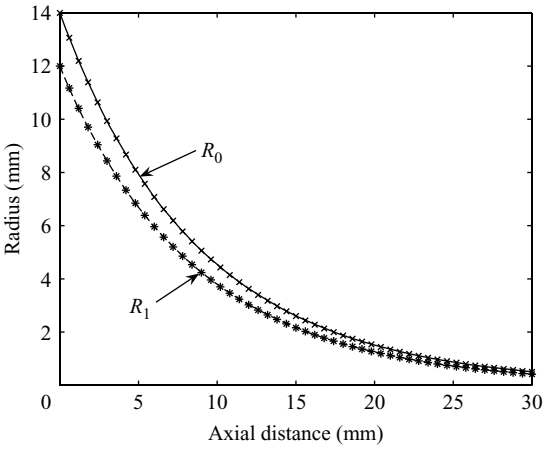

FIGURE 3. Numerically and analytically obtained variation of inner and outer radii with axial distance.

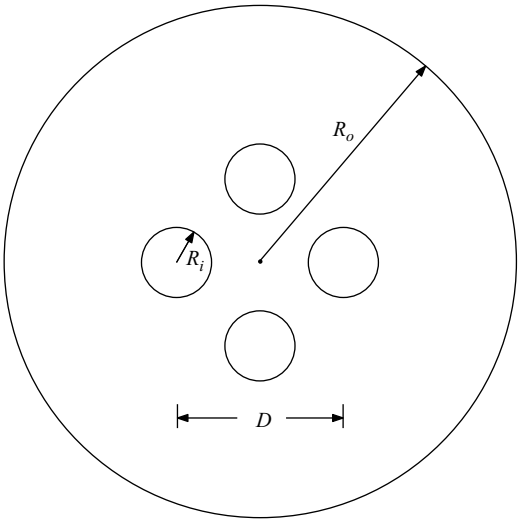

FIGURE 4. Schematic of a fibre containing four circular holes, showing the geometric parameters.

5.2. *Cross-section with four circular holes*

Next we consider a geometry with a circular cross-section containing four circular holes of equal radii. Figure 4 shows a schematic of a cross-section containing four holes of equal radii. Different scenarios are considered where the effects of surface tension, viscosity, inertia, gravity and internal pressurization are examined. Finally, the effect of draw speed (draw force) and feed speeds are examined. All the hole boundaries are discretized using 125 points, and once again, the maximum deviation from mass conservation was found to be less than 1 % in all cases simulated.

5.2.1. *Four close holes with surface tension, no inertia and gravity*

The simplest case to be studied is obtained by neglecting axial inertia and gravity terms or by setting $Re = 0$ and $St = 0$. Figure 5 shows the neck-down profile of a four-hole structure with $F_d = 2.0$ N and a feed speed $U_f = 2\,\mathrm{mm\,min^{-1}}$, also showing initial

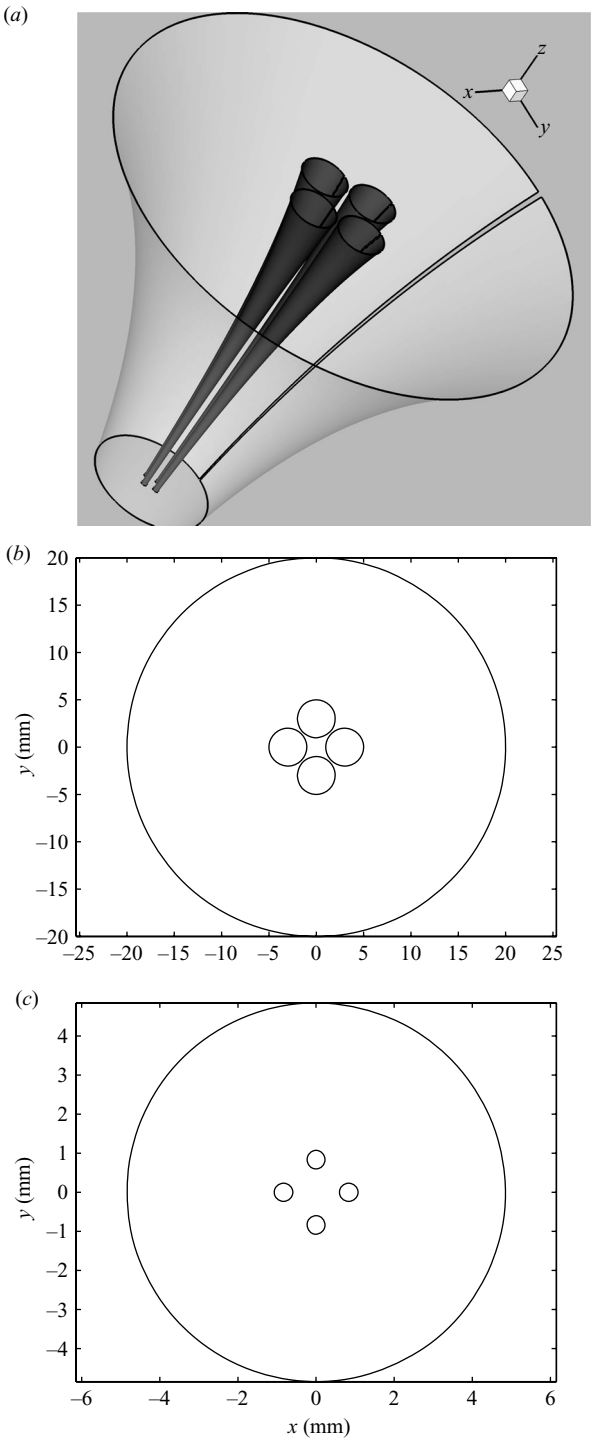

FIGURE 5. Neck-down profile of a fibre with four holes: (*a*) Neck-down profile; (*b*) Initial cross-section, $z = 0$; and (*c*) final cross-section, $z = L$. $Ca = 62.1 \times 10^3$ for (*a*) and 62.1×10^4 for (*b*) and (*c*).

and final geometries after a draw length of 30 mm. We can define a non-dimensional number similar to that of Fitt *et al.* (2002), to characterize the change in the size of the holes. We define a collapse ratio

$$C_\alpha = 1 - \sqrt{\frac{(A_\alpha(z)/A_0(z))}{(A_a(0)/A_0(0))}}, \tag{5.4}$$

such that $C_\alpha = 0$ when the fibre evolves in a self-similar manner and $C_\alpha = 1$ when the holes completely collapse and negative values indicate hole expansion. It should be noted here that hole expansion is not anticipated except in the presence of internal pressurization. The form of the collapse ratio is chosen such that it reduces to the form proposed by Fitt *et al.* (2002) when the hole shape remains the same throughout the draw (e.g. the axisymmetric case). The variation of the collapse ratio along the length gives an indication of the nature of the physical parameters in the problem. From (2.21) it can be seen that the surface tension contribution to the total force depends on the total circumference and the viscous stress contribution is dependent on the product of the area and the axial velocity gradient. When the velocity gradients are large, the viscous stresses dominate the evolution of the cross-section of the fibre. The surface tension effects on the collapse ratio will be dominant only in the initial portion of the draw when the circumference is large and the velocity gradients are small. Finally, increasing the draw tension increases the initial velocity gradient, decreasing the effect of surface tension and vice versa. It should be noted here that Fitt *et al.* (2001, 2002) also observed that collapse due to surface tension was dominant only in the initital part of the drawing. Similar to the expression of Fitt *et al.* (2001, p. 1929), the sensitivity of the collapse ratio to the different physical parameters in the problem can be expressed as

$$C_\alpha \propto \frac{\gamma L}{\mu U_f \ln(U/U_f)}. \tag{5.5}$$

Numerical experiments were performed to examine the effect of surface tension and viscosity and draw tension on the collapse ratio. Simulations were stopped if a predetermined draw ratio was reached, a predetermined maximum length was reached, or if there was a complete hole collapse. The effects of viscosity and surface tension were analysed using the capillary number ($Ca = \mu U/\gamma$), by systematically changing the viscosity and the surface tension, keeping the draw tension (and the initial velocity gradient) and the feed speed constant. In figure 5, the x-axis represents the instantaneous draw ratio during the drawing and should not be interpreted as the final draw ratio at the end of the draw. Figures 6*a* and 6*b* show the variation of the collapse ratio with the draw ratio for different values of the Ca varying over two orders of magnitude. First, we examine the effect of changing the viscosity. In figure 6*a*, Ca is varied by keeping the surface tension constant and changing the viscosity. Decrease in Ca values implies a decrease in the viscosity and vice versa. It can be seen that the collapse ratio is significantly affected by this ratio and C_α increases with increasing Ca when the viscosity is kept constant. However, the collapse ratio asymptotically approaches some constant value and the draw ratio at which this asymptotic value is reached remains approximately constant and independent of Ca. From (2.21) we see that for constant draw tension and constant surface tension, the velocity gradient decreases with increasing viscosity (increasing Ca). Thus, the sintering effects increase with increasing viscosity in the intial stages of the draw, as can be clearly seen in figure 6*a*. As the drawing progresses, the velocity gradient

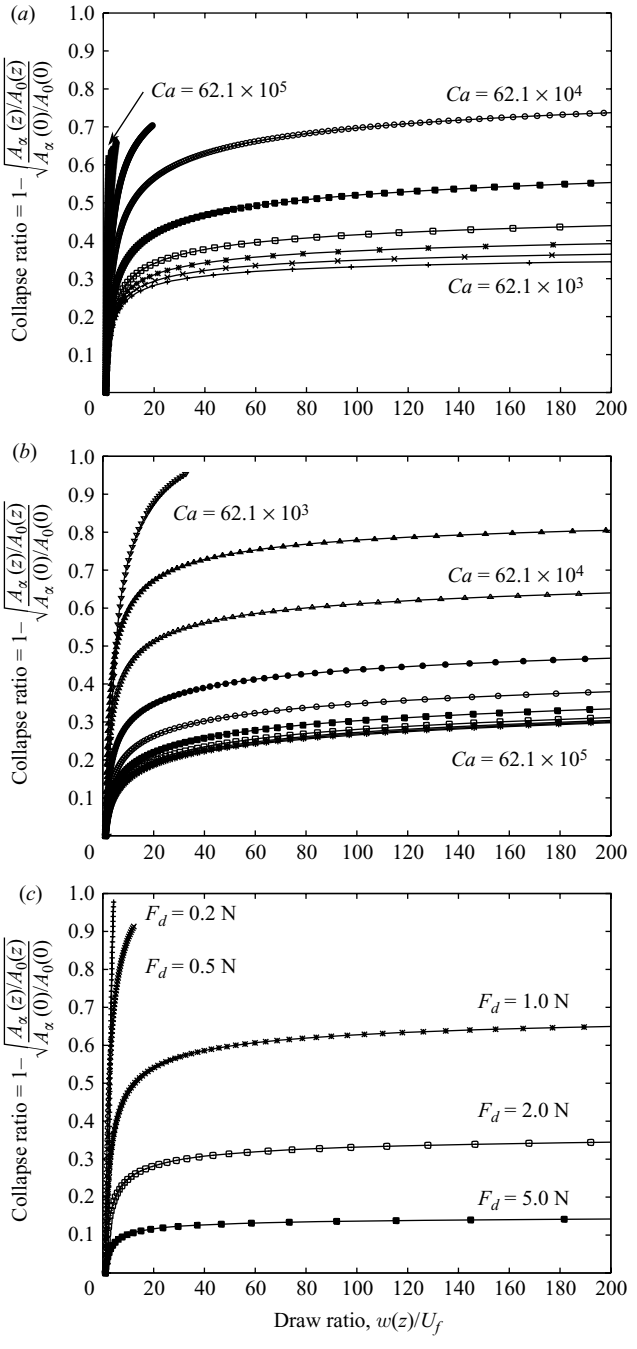

FIGURE 6. Variation of collapse ratio for one of the inner holes with draw speed: (*a*) variation of collapse ratio for different *Ca* values; (*b*) variation of collapse ratio with *Ca*, keeping viscosity constant; and (*c*) variation of collapse ratio for different draw tensions.

increases and the total circumference decreases, increasing the effect of viscosity and reducing that of surface tension. Figure 6*b* shows the effect of changing surface tension on the collapse ratio. As one would expect, we can see that the collapse ratio increases with decreasing *Ca* (or increasing surface tension). It can be seen that

the collpase ratio is strongly coupled to the velocity gradient, viscosity and surface tension. It should be noted here that the results are seemingly in contradiction to the prediction of (5.5). This is because the draw length required to prduce a given draw ratio is not constant in figure 6*a*. By fixing the draw tension and surface tension, the length required to produce the desired draw ratio increases with increasing viscosity. Validity of (5.5a) was confirmed by performing a series of simulations in which the draw length, draw ratio and surface tension were held constant and the viscosity was varied. These results are not presented here for brevity. Figure 6*b* shows the effect of surface tension on the collapse ratio. The collapse ratio increases with decreasing Ca (or increasing surface tension), consistent with (5.5). The variation of C_α with viscosity can also be interpreted in terms of the non-dimensional draw tension ($\overline{F_d}$) defined in (2.22). We see that with a constant applied tension, increasing viscosity decreases $\overline{F_d}$ and the initial velocity gradients, thereby increasing the effects of surface tension.

To examine the effects of the changes in the initial velocity gradient, the draw tension was varied systematically, keeping Ca and the feed speed constant. Figure 6*c* shows the variation of $C_\alpha$with the draw ratio for different values of the draw tension, with constant surface tension and viscosity. Increasing the draw tension increases the initial velocity gradient, thereby reducing the surface tension effects, causing a drop in the asymptotic value of C_α. Increasing the draw tension decreases the length over which the desired draw ratio is achieved and vice versa. Figures 6*a* and 6*b* can also be interpreted in terms of required length of the hot zone to produce a particular draw ratio. In figure 6*a*, the draw length required for the final draw ratio of 200 increases from 6 mm to the set maximum of 60 mm, thus suggesting that surface tension effects are more apparent in a drawing process with lower axial velocity gradients. Thus, in a high-temperature (low-viscosity, low-Ca) process with a short draw length, very good control can be achieved over the final dimensions of the fibre and the holes, and numerical modelling of the process can be restricted to only a short portion of the draw. However, when the draw length is longer and draw forces are moderate, the entire process needs to be simulated to obtain predictions of the final dimensions of the fibre and the holes.

We can also look at hole deformation of the closely spaced holes, since the final shape of the holes can play an important role in determining the optical properties of the fibre. Figure 7 shows the hole deformations for two different capillary numbers, plotted at the same draw ratio, drawn over the same length of 60 mm. The change in Ca in figure 7*a* is obtained by keeping the surface tension constant, and in figure 7*b* the visccosity is kept constant. In figure 7b, the attention is resricted to the single hole with its centre on the negative x-axis, and the values are normalized to the original hole size. We observe in figure 7*a* that decrease in viscosity or increase in Ca causes shape change. The hole-shape change with viscosity is related to the velocity gradient at the given cross-section, and we obtain increasing shape change with increasing velocity gradient or, in other words, increasing the draw tension will cause greater shape change. The non-dimensional draw tension ($\overline{F_d}$) is a good indicator of the hole-shape change, with higher values of $\overline{F_d}$ causing greater shape change. Independent simulations with different draw tension values have confirmed this. In figure 7*b*, we observe that there is almost no change in shape, with a decrease in diameter caused by surface tension.

In the example problem considered thus far, the outward surface normals have been oriented pointing away from the centroid of the hole and we will refer to these surfaces as convex. In completing the study of surface tension and viscosity effects, we

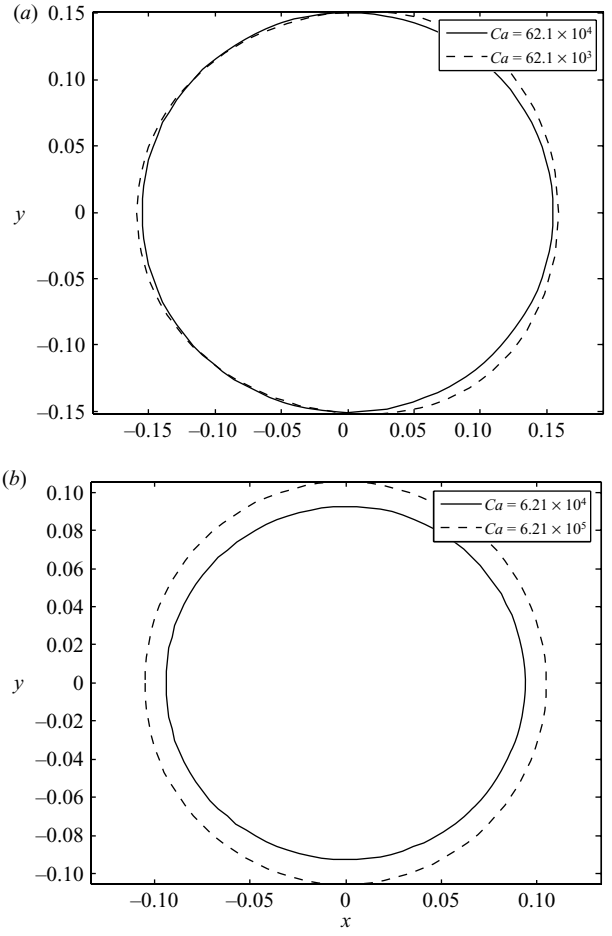

FIGURE 7. Hole deformation for two different Capillarity numbers, draw ratio = 200: (*a*) shape change with change in viscosity and (*b*) shape change with change in surface tension.

will finally deal with a shape that is concave (outward normal is oriented towards the centroid) in portions, and also illustrate that the model can handle arbitrarily shaped cross-sections. Figure 8*a* shows the evolution of a star, shaped hole, with figures 8*b*, 8*c* and 8*d* showing the evolution of the cross-section at different axial distances. Here, the star-shaped holes evolve towards a circular hole. The change in shape is caused mainly by the viscous stresses. Although the final shape and size of the star-shaped hole is affected by surface tension, we observe a similar transition to circular holes even for the case with 0 surface tension. This example just serves to illustrate that the model is capable of prediciting deformation of complicated structures with relatively large in-plane curvatures.

5.2.2. *Four close holes, with surface tension, axial inertia and axial gravity*

Axial inertia and gravity are easily included into the solution procedure if a good estimate of the first derivative of the axial velocity ($w_z(z=0)$) is available. If the draw force F_d is provided a simple Newton–Raphson iterative scheme is used to estimate w_z at the start (see, for example, Press *et al.* 2002). Figure 9 shows the effects of gravity and inertia on the collapse ratio, by comparing the variation of collapse ratio to the

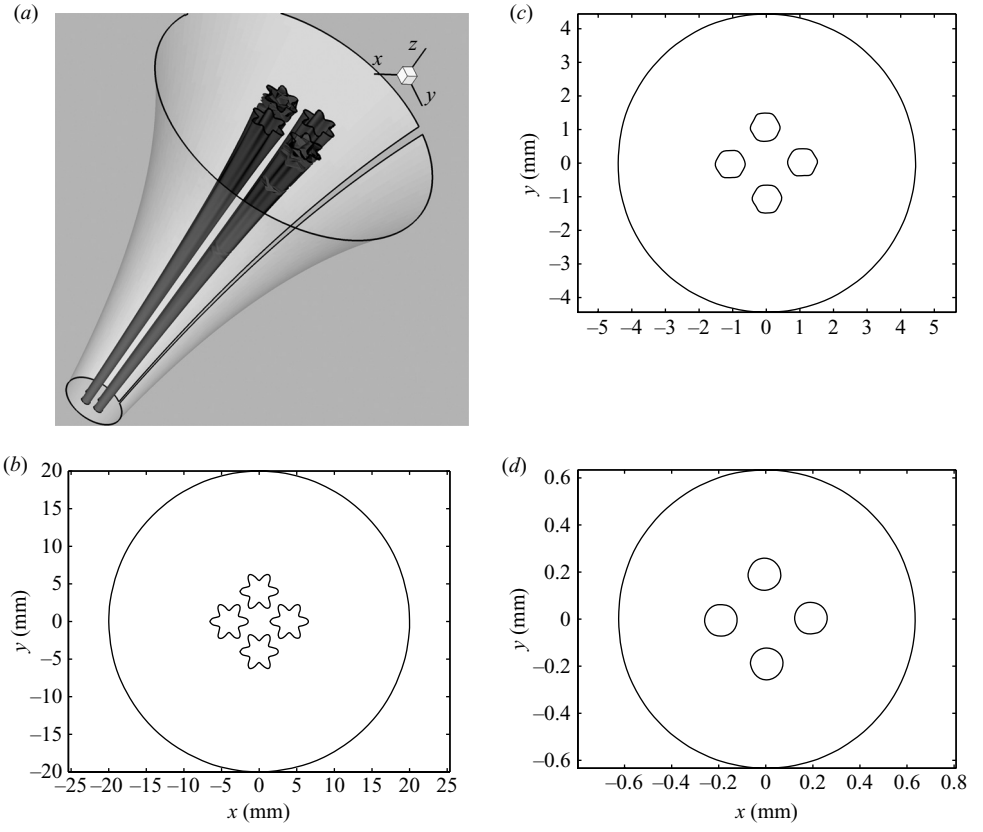

FIGURE 8. Neck-down profile for fibre with four star-shaped holes, $Ca = 1.61 \times 10^4$: (*a*) neck-down profile, (*b*) initial cross-section, (*c*) shape at one-half length and (*d*) final cross-section.

no gravity and inertia solution for the example of four close circular holes of figure 4. It can be seen that the collapse ratio is reduced by inertia and gravity because the gravitational and inertial effects act like additional axial forces at least when gravity is acting in the draw down direction. An opposite effect is expected when gravity is acting against the draw down direction. Inertial effects are not expected to be important except when very low draw tensions are used or high feed speeds or when the fibre is very dense.

5.2.3. *Four close holes with internal pressurization*

Internal pressurization is already included into the solution procedure as it is included in defining $g(t_o)$ in (3.12). Numerical simulations were performed by keeping the external hole overpressure equal to a constant value on all the holes. The numerical results are obtained keeping $Ca = 62.1 \times 10^4$ and $St = 0$ and $Re = 0$ corresponding the example of four circular holes in figure 6 with $F_d = 2.0$ N. Figure 10 shows the variation of the collapse ratio for different values of the non-dimensional pressure, corresponding to 0, 10 and 70 Pa of the dimensional hole overpressure. As indicated by the scaling defined in § 2, it can be seen that the process is extremely sensitive to the hole overpressure and it has to be within $O(\epsilon^2)$ of the ambient pressure to avoid complete explosion of the holes. It can be seen that collapse can be avoided and with a careful control of the hole overpressure will lead to conditions of self-similar drawing

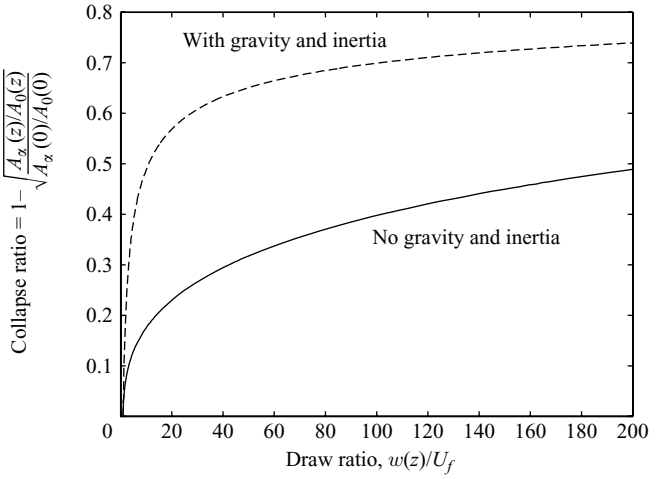

FIGURE 9. Axial gravity and inertia effects: $Re = 1$, $St = 1$ and $Ca = 62.1 \times 10^4$.

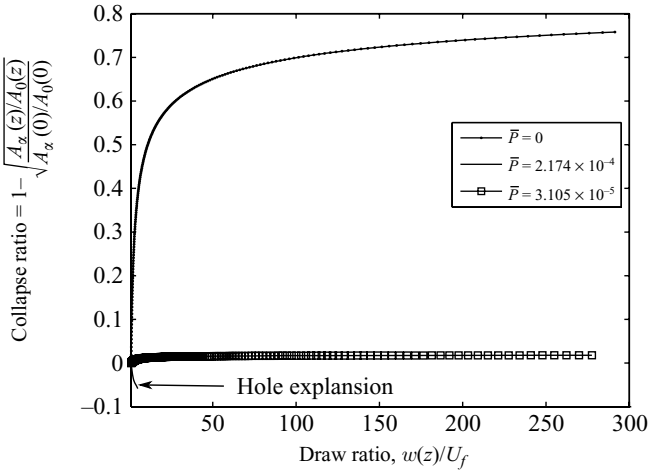

FIGURE 10. Variation of collapse ratio with draw ratio for different values of the internal pressurization: $Re = 0$, $St = 0$ and $Ca = 62.1 \times 10^4$.

($C^\alpha = 0$). Initially, when the holes are large, the pressurization plays an important role in controlling the evolution of the cross-section.

6. Non-Isothermal drawing

Thus far, we have assumed that the temperature and, as a consequence, the material properties remain constant throughout the drawing process in order to simplify the mathematical analysis. In reality, all the material parameters, ρ, μ and γ, are functions of temperature. For most practical applications, μ changes by several orders of magnitude for relatively modest changes in temperature, and all the other material properties are only weak functions of the temperature. In proceeding with a mathematical description of a non-isothermal drawing process, we assume that only μ alone is a function of temperature and all the other parameters are independent of the temperature. Also, we are interested only in the temperature distribution to

determine its effect on the viscosity. So, here we do not attempt to solve the energy equation but assume that a temperature distribution is provided. As before, we start with the incompressible Navier–Stokes equations

$$\nabla \cdot \boldsymbol{q} = 0, \tag{6.1a}$$

$$\rho[\mathbf{q}_t + \mathbf{q} \cdot \nabla \boldsymbol{q}] = -\nabla p + \nabla \cdot (2\mu \mathbf{E}) + \mathbf{F}, \tag{6.1b}$$

where $\mathbf{E}_{ij} = 1/2(\partial u_i/\partial x_j + \partial u_j/\partial x_i)$. The boundary conditions for the Navier–Stokes equations are identical to (2.3), and the kinematic condition is identical to (2.2). We now expand the variables including the temperature as an asymptotic series in even powers of ϵ. In addition, we assume a functional dependence for the temperature, such that $\bar{T} = \bar{T}_0(\bar{z}, \bar{t}) + \epsilon^2 \bar{T}_1(\bar{x}, \bar{y}, \bar{z}, \bar{t}) + O(\epsilon^4) + \cdots$. Small Biot number is required for the in-plane temperature variation to be small (Wylie, Huang & Miura 2007). From this assumption, the temperature (and thus the viscosity) is independent of x and y up to leading order. We introduce a non-dimensional viscosity $\bar{\mu} = \mu/\mu_R$, where μ_R is the viscosity at some reference temperature T_R and a non-dimensinal temperature $\bar{T} = T/T_R$. Therefore, the non-dimensional viscosity can be expressed as $\bar{\mu} = \bar{\mu}_0 + \epsilon^2 \bar{\mu}_1 + O(\epsilon^4)$. The dimensionless parameters are redefined with respect to the reference viscosity μ_R so that the Reynolds, Capillarity and Stokes numbers are now given by

$$Re = \frac{\rho U L}{\mu_R}, \; Ca = \frac{\mu_R U}{\gamma_R} \text{ and } St = \frac{\rho L^2 g}{\mu_R U}.$$

Non-dimensionalizing and expanding the dependent variables as an asymptotic series, the leading-order flow equations are identical to (2.8). The $O(\epsilon^2)$ equations for the axial momentum and boundary conditions are

$$\mu_0 \left[w_{1xx} + w_{1yy}\right] = Re\,[w_{0t} + w_0 w_{0z}] + p_{0z} - (\mu_0 w_{0z})_z - \mu_0 w_{0z} - St\cos\beta \text{ in } D, \tag{6.2a}$$

$$\mu_0 \left[w_{1x} G_{0x} + w_{1y} G_{0y}\right] = G_{0z}(p_0 - 2\mu_0 w_{0z} - \bar{\gamma}\kappa_0) - \mu_0 u_{0z} G_{0x} - \mu_0 v_{0z} G_{0y} \text{ on } \partial G^{\alpha} = 0. \tag{6.2b}$$

Applying the solvability criterion to (6.2) and some involved manipulations, we obtain the axial force balance equation for a non-isothermal process as

$$(3\mu_0 A w_{0z})_z = ReA(w_{0t} + w_0 w_{0z}) - StA - \frac{1}{2}\bar{\gamma}\Gamma_{0z}. \tag{6.3}$$

It can be seen that (6.3) is very similar to (2.20), with the exception that the viscosity appears inside the derivative on the left-hand side. For a given temperature distribution, the values of μ_0 and its derivative are known and the solution process described in § 4 can be applied to solve the non-isothermal problem without difficulty.

7. Conclusions

The leading-order equations governing the evolution of slender viscous fibres with the cross-section containing holes, during axial stretching under the influence of surface tension, axial gravity, inertia and internal pressurization were derived. The derivation follows earlier works of Dewynne *et al.* (1992) and Cummings & Howell (1999) where the cross-section was simply connected and generalizes the equations to multiply connected cross-sections. This process then decouples the Navier–Stokes equations to the solution of two problems: one of an in-plane Stokes flow problem

with surface tension-or pressure-driven free boundaries, coupled with a kinematic condition that governs the evolution of the cross-section. The solution to the problem is obtained numerically by repeatedly solving the S–L equation for the Stokes flow problem and advancing the cross-section in space (and time) using the kinematic condition. The solution presented here is restricted to cross-sections that had a certain symmetry such that the centreline of the fibre did not translate or rotate and when no initial twist or translation has been applied to the fibre. The model for isothermal drawing was extended to include non-isothermal effects, which are inherent in any real microstructured optical fibre drawing. This solution procedure represents a huge simplification to solving the full three-dimensional Navier–Stokes free-boundary problem.

Sample numerical solutions were computed for a geometry containing four closely spaced holes, and effects of surface tension, inertia, gravity and internal pressurization were determined. It was found that surface tension has a large effect on the final geometry of the fibre. However, depending on the final velocity and the initial velocity derivative (or draw tension), surface tension effects were important only for some portion of the drawing process following which self-similar evolution was observed. The collapse ratio was defined to characterize this effect and also to characterize the degree of sintering. Hole-shape change is primarily governed by the non-dimensional draw tension, with higher values producing greater shape change. It was also found that inertia and gravity did not affect the shape of the holes but played an important role in determining the degree of sintering in the process. Finally, internal pressurization had a significant effect on the shape and size of the holes and it was also determined that the hole overpressure has to be within $O(\epsilon^2)$ so that the holes do not explode.

In this paper, we have drawn from previous literature on two-dimensional viscous sintering and the evolution of slender solid fibers and extended these ideas to predict the evolution of fibres with holes in the cross-section. Due to the explicit nature of the solution procedure, one of the significant engineering advantages is the ability to reverse engineer a preform for a given final fibre geometry and drawing conditions, thereby reducing the effort involved in preform preparation, which is considered to be the most expensive part of optical fibre fabrication. Some possible extensions to our work are to quantify effects in the three-dimensional sintering of closely packed cylinders and other shapes.

Funding from the National Science Foundation is gratefully acknowledged. We also thank Prof. Horea Illies for many useful discussions during the development of the numerical scheme and Prof. Eric Jordan for critically reading the manuscripts and suggesting many useful improvements.

REFERENCES

Birks, T. A., Knight, J. C. & Russell, P. St. J. 1997 Endlessly single-mode photonic crystal fibre. *Opt. Lett.* **22**, 961–963.

Birks, T. A., Roberts, P. J., Russell, P. J., Atkin, D. M. & Shepherd, T. J. 1995 Full 2-d photonic band gaps in silica/air structures. *Electron. Lett.* **31**, 1941–1942.

Bise, R. T., Trevor, D. J., Monberg, E. & DiMarcello, F. 2002 Impact of preform fabrication and fiber draw on the optical properties of microstructured fibers. In *Proc. of the 51st IWCS*, pp. 339–343.

Cheng, X. & Jaluria, Y. 2002 Effect of draw furnace geometry on high-speed optical fiber manufacturing. *Num. Heat Trans. A Fundam.* **41**, 757–781.

Choudhury, S. Roy & Jaluria, T. 1998 Practical aspects of drawing an optical fiber. *J. Mater. Res.* **13** 483–493.

Crowdy, D. 2002 Exact solutions for the visocus sintering of multiply-connected fluid domains. *J. Engng Math.* **42**, 225–242.

Cummings, L. J. & Howell, P. D. 1999 On the evolution of non-axisymmetric viscous fibres with surface tension, inertia and gravity. *J. Fluid Mech.* **389**, 361–389.

Dewynne, J. N., Ockendon, J. R. & Wilmott, P. 1992 A systematic derivation of the leading-order equations for extensional flows in slender geometries. *J. Fluid Mech.* **244**, 323–338.

Dewynne, J., Ockendon, J. R. & Wilmott, P. 1994 On a mathematical-model for fiber tapering. *Q. J. Mech. Appl. Math.* **47**, 541–555.

Fitt, A. D., Furusawa, K., Monro, T. M. & Please, C. P. 2001 Modeling the fabrication of hollow fibers: Capillary drawing. *J. Lightwave Technol.* **19** (12), 1924–1931.

Fitt, A. D., Furusawa, K., Monro, T. M., Please, C. P. & Richardson, D. J. 2002 The mathematical modelling of capillary drawing for holey fiber manufacture. *J. Engng Math.* **43**, 201–227.

Gospodinov, P. & Yarin, A. L. 1997 Draw resonance of optical microcapillaries in non-isothermal drawing. *Int. J. Multiphase Flow* **23** (5), 967–976.

Greengard, L., Kropinski, M. C. & Mayo, A. 1996 Integral equation methods for stokes flow and isotropic elasticity in the plane. *J. Comput. Phys.* **125** (2), 403–414.

Hopper, R. W. 1990 Plane Stokes flow driven by capillarity on a free surface. *J. Fluid Mech.* **213**, 349–375.

Howell, P. D. & Siegel, M. 2004 The evolution of a slender non-axisymmetric drop in an extensional flow. *J. Fluid Mech.* **521**, 155–180.

Lu, J.-K. 1995 *Complex Variable Methods in Plane Elasticity*. World Scientific.

Matovich, M. A. & Pearson, J. R. A. 1969 Spinning a molten threadline – steady-state isothermal flows. *Ind. Engng Chem. Fundam.* **8**, 512–520.

Mikhailov, V. N. 1979 Plane problem of the theory of elasticity in multiply-connected domains with cyclic and mirror symmetry. *J. Appl. Math. Mech. (English translation of Prikladnaya Matematika i Mekhanika)* **43** (2), 401–404.

Muskhelishvili, N. I. 1963*a* *Singular Integral Equations: Boundary Problems of Function Theory and Their Application to Mathematical Physics*. Groningen, P. Noordhoff.

Muskhelishvili, N. I. 1963*b* *Some Basic Problems of the Mathematical Theory of Elasticity: Fundamental Equations, Plane Theory of Elasticity, Torsion, and Bending*. Groningen, P. Noordhoff translation of the 4th corrected and augmented edition, Moscow, 1954.

Paek, U. C. & Bunk, R. B. 1978 Physical behavior of the neck-down region during furnace drawing. *J. Appl. Phys.* **49**, 4417–4422.

Press, W. H., Teukolsky, S. A., Vetterling, W. T. & Flannery, B. P. 2002 *Numerical Recipes in C*. Cambridge University Press.

Richardson, S. 1992 Two-dimensional slow viscous flows with time-dependent free boundaries driven by surface tension. *Eur. J. Appl. Math.* **3**, 193–207.

Richardson, S. 2000 Plane stokes flows with time-dependent free boundaries in which the fluid occupies a doubly-connected region. *Eur. J. Appl. Math.* **11**, 249–269.

Russell, P. 2003 Photonic crystal fibers. *Science* **299**, 358–362.

Sarboh, S. D., Milinkovic, S. A. & Debeljkovic, D. L. J. 1998 Mathematical model of the glass capillary tube drawing process. *Glass Technol.* **39**, 53–67.

Schultz, W. W. & Davis, S. H. 1982 One-dimensional liquid fibers. *J. Rheol.* **24** (4), 331–345.

Shah, Y. Y. & Pearson, J. R. A. 1972 On the stabiloty of nonisothermal fiber spinning. *Ind. Engng Chem. Fundam.* **11**, 145–149.

Tanveer, S. & Crowdy, D. G. 1998 A theory of exact solutions for plane viscous blobs. *J. Nonlinear Sci.* **8**, 261–279.

Tanveer, S. & Vasconcelos, G. L. 1994 Bubble breakup in two-dimensional Stokes flow. *Phys. Rev. Lett.* **73** (21), 2845–2848.

Tanveer, S. & Vasconcelos, G. L. 1995 Time-evolving bubbles in two-dimensional Stokes flow. *J. Fluid Mech.* **301**, 325–344.

Thompson, J. F. 1985 *Nummerical grid generation: Foundations and Applications*. Elsevier Science Publishing Co., Inc.

Vorst, G. A. L. van de 1993 Integral method for a two-dimensional stokes flow with shrinking holes applied to viscous sintering. *J. Fluid Mech.* **257**, 667–689.

Wylie, J. J., Huang, H. & Miura, R. M. 2007 Thermal instability in drawing viscous threads. *J. Fluid Mech.* **570**, 1–16.

Xue, S. C., Large, M. C. J., Barton, G. W., Tanner, R. I., Poladian, L. & Lwin, R. 2006 Role of material properties and drawing conditions in the fabrication of microstructured optical fibers. *J. Lightwave Technol.* **24** (2), 853–860.

Xue, S. C., Tanner, R. I., Barton, G. W., Lwin, R., Large, M. C. J. & Poladian, L. 2005*a* Fabrication of microstructured optical fibers – part II: Numerical modeling of steady-state draw process. *J. Lightwave Technol.* **23** (7), 2255–2266.

Xue, S. C., Tanner, R. I., Barton, G. W., Lwin, R., Large, M. C. J. & Poladian, L. 2005*b* Fabrication of microstructured optical fibers – part I: Problem formulation and numerical modeling of transient draw process. *J. Lightwave Technol.* **23** (7), 2245–2254.

Yarin, A. L., Gospodinov, P. & Roussinov, V. I. 1994 Stability loss and sensitivity in hollow fiber drawing. *Phys. Fluids* **6**, 1454–1463.

Yin, Z. & Jaluria, Y. 2000 Neck down and thermally induced defects in high speed optical fiber drawing. *J. Heat Transf.* **122**, 351–362.